Advances in Nano Research, *Vol. 15, No. 1 (2023) 1-13*
https://doi.org/10.12989/anr.2023.15.1.001

Calcium annealing approach to control of surface groups and formation of oxide in $Ti_3C_2T_x$ MXene

Jung-Min Oh[1†], Su Bin Choi[2†], Taeheon Kim[3], Jikwang Chae[1], Hyeonsu Lim[4],
Jae-Won Lim[3], In-Seok Seo[**3] and Jong-Woong Kim[*2,5]

[1]R&D center, INNOMXENE Co.,Ltd., 66, Daehwa-ro 106beon-gil, Daedeok-gu, Daejeon 34365, Republic of Korea
[2]Department of Smart Fab Technology, Sungkyunkwan University, 2066 Seobu-ro, Jangan-gu,
Suwon, Gyeonggi-do 16419, Republic of Korea
[3]School of Advanced Materials Engineering, Jeonbuk National University, 567 Baekje-daero, Deokjin-gu, Jeonju 54896, Republic of Korea
[4]Department of Strategy Planning, Jeonbuk Institute of Automotive Convergence Technology, 6,
Dongjansan 2-gil, Gunsan 54158, Republic of Korea
[5]School of Mechanical Engineering, Sungkyunkwan University, 2066 Seobu-ro, Jangan-gu, Suwon,
Gyeonggi-do 16419, Republic of Korea

(*Received July 26, 2021, Revised March 6, 2023, Accepted March 7, 2023*)

Abstract. $Ti_3C_2T_x$ MXene, a 2D material, is known to exhibit unique characteristics that are strongly dependent on surface termination groups. Here, we developed a novel annealing approach with Ca as a reducing agent to simultaneously remove F and O groups from the surface of multilayered MXene powder. Unlike H_2 annealing that removes F effectively but has difficulty in removing O, annealing with Ca effectively removed both O and F. X-ray photoelectron spectroscopy (XPS) and energy dispersive X-ray spectroscopy revealed that the proposed approach effectively removed F and O from the MXene powder. The results of O/N analyses showed that the O concentration decreased by 57.5% (from 2.66 to 1.13 wt%). In addition, XPS fitting showed that the volume fraction of metal oxides (TiO_2 and Al_2O_3) decreased, while surface termination groups (–O and –OH) were enhanced, which could increase the hydrophilic and adsorption properties of the MXene. These findings suggest that when F and O are removed from the MXene powder, the interlayer spacing of its lattice structure increases. The proposed treatment also resulted in an increase in the specific surface area (from 5.17 to 10.98 m^2/g), with an increase in oxidation resistance temperature in air from ~436 to ~667 °C. The benefits of this novel technology were verified by demonstrating the significantly improved cyclic charge–discharge characteristics of a lithium-ion battery with a Ca-treated MXene electrode.

Keywords: deoxidation; lithium-ion battery; MXene; surface termination group; $Ti_3C_2T_x$

1. Introduction

Since the discovery of single-layer graphene, two dimensional (2D) materials have received considerable attention because of their unique properties compared to their bulk counterparts (Nejadi *et al.* 2021, Cai *et al.* 2022). Recently, MXene 2D materials have attracted attention due to their hydrophilic surfaces and high metallic conductivities (Naguib *et al.* 2011, Cai *et al.* 2021), which have enabled promising performance in diverse applications, including transparent electrodes (Zhang *et al.* 2017, Chen *et al.* 2020, Ahn *et al.* 2020), supercapacitors (Jiang *et al.* 2018, Zhu *et al.* 2016, Fan *et al.* 2018), bio sensors (Liu *et al.* 2019), water desalination (Fan *et al.* 2020, Malik 2018, Ihsanullah 2020), electromagnetic interference shielding (Shahzad *et al.* 2016, Iqbal *et al.* 2020, Yun *et al.* 2020), radioactive substance treatment (Hwang *et al.* 2020), and lithium-ion batteries (Hwang *et al.* 2019). MXene is comprised of transition-metal carbides, carbonitrides, or nitrides with a general formula of $M_{n+1}X_n$, where M represents transition metals (such as Ti, Sc, Zr, Hf, V, Nb, Ta, Cr, Mo, etc.) and X is carbon and/or nitrogen (Cai *et al.* 2022). For example, Ti_3C_2 is a representative MXene phase, which is fabricated by the selective etching of the A layer from its precursor MAX phase using a highly acidic (HF or HCl-based) solution. Al (or Si) has been used as a material for the A layer in the MAX (Gogotsi and Anasori 2019, Feng *et al.* 2022), resulting in the Ti_3AlC_2 phase. The removal of Al from the Ti_3AlC_2 phase by aqueous chemical methods leads to the formation of MXene ($M_{n+1}X_nT_x$) and its multilayered accordion-like structures (Gogotsi and Anasori 2019). Here, T_x refers to surface-termination groups.

The $Ti_3C_2T_x$ MXene has a very high specific surface area (SSA) (Yan *et al.* 2021, Fen *et al.* 2022). In combination with its conductive core and hydrophilic surface, the high SSA enables this material to bind various cations between the layers of the MXene structure. This implies that the MXene can be used as a key material in various energy-storage devices (Natu *et al.* 2018, Dong *et al.* 2018, Zhang and Nicolosi 2019). It is also known that multilayered MXene has one of the largest known volumetric capacitances (520 F/cm^3 at 2 mV/s) and therefore can be used as an electrical-double-layer capacitor

---

*Corresponding author, Professor,
E-mail: wyjd@skku.edu
**Co-corresponding author, Professor,
E-mail: isseo@jbnu.ac.kr

†These authors equally contributed to this work

http://www.techno-press.org/?journal=journal=anr&subpage=5
ISSN: 2287-237X (Print), 2287-2388 (Online)

(Dall'Agnese *et al.* 2014). Therefore, it is advantageous to increase the SSA to improve MXene performance. In multilayered MXene, control of the SSA is performed after producing the accordion-like structures. The SSA of the multilayered MXene can be increased via mechanical methods, such as sonication or shaking (Munir *et al.* 2020); these methods increase the inter-layer distance through intercalation with ions or guest molecules (Wen *et al.* 2017), physical adsorption or covalent bonding with guest molecules or nanoparticles (Wang *et al.* 2018), and/or complexing with other 2D nanomaterials (Shen *et al.* 2017, Yan *et al.* 2020). It is very difficult to precisely control the SSA through mechanical methods alone. However, alternative methods require the introduction of other materials, which can affect other properties of the MXene in addition to the SSA.

In addition, the etching of the MAX phase with an aqueous medium in HF solutions results in a variety of surface terminations, such as fluorine (–F), oxygen (–O) and hydroxyl (–OH) groups (Gogotsi and Anasori 2019). Since the discovery of MXene materials, many research groups have reported that the surface terminations significantly affect the electronic and adsorption properties of the MXene (Hu *et al.* 2018, Schultz *et al.* 2019). Schultz *et al.* (2019) reported that F solely occupies the face-centered cubic (FCC) adsorption sites of MXene surfaces, affecting the work function. In particular, in the case of lithium-ion batteries, it was found that F on the surface of MXene adversely affects the adsorption of lithium ions (Lu *et al.* 2019, Rakhi *et al.* 2015). Similarly, O on the surface of MXenes can generate TiO_2, which increases the contact resistance and consequently degrades the electrical performance (Lee *et al.* 2020). In addition, other researchers have noted that when MXene is used as an adsorbent for radioactive substances, the MXene can release the absorbed radioactive substances in the presence of O on the surface (Hwang *et al.* 2020).

In recent studies, high-temperature annealing was performed under vacuum or H_2 gas to remove F from the surface of MXene (Rakhi *et al.* 2015, Kong *et al.* 2018). While F was effectively removed by these methods, O remained or increased in concentration in the worst case. For this reason, it is necessary to develop a process that can simultaneously remove F and O from the MXene surfaces. Since Ti and its compounds readily react with O and generate a TiO_2 oxide layer on the surface, there have been an attempt to prevent this oxidation process (Oh *et al.* 2014). The solution requires reducing Ti and its compounds to remove O via reactions with Ca, Mg, or Al, which have higher affinity for O than Ti. Herein, we demonstrate a novel Ca reduction process to remove F and O from the surface of $Ti_3C_2T_x$ MXene. We also investigated the effect of Ca treatment on the SSA of multilayered MXene. In addition, the lattice parameters and thermal properties of the multilayered MXene powders were examined according to the concentrations of F and O. We compared the effect of Ca treatment with that of H_2 annealing on the MXene properties. To verify the applicability of the proposed method, we applied the MXene before and after Ca treatment to a lithium-ion battery and evaluated the changes in the cyclic charge–discharge characteristics.

2. Experimental section

2.1 Preparation of Ti_3AlC_2 MAX precursor and multi-layered MXene powder

To prepare the Ti_3AlC_2 precursor, commercially available Ti (99.9%), Al (99.9%), and C powder from High Purity Chemical (Japan) were used as starting materials, and were mixed with a molar ratio of 3:1:2 in a planetary ball mill. Then, a graphite die with the powder mixture was placed in a spark plasma sintering (SPS) furnace and sintered at 1100 °C for 10 min under vacuum (9.8×10^{-3} Pa) with a pressure of 60 MPa. The sintered powder was heat treated at 1400 °C for 2 h under vacuum of 6.7×10^{-3} Pa and ground to a powder with a 10-µm mean particle size. To prepare the MXene powder, 1 g of synthesized precursor powder with Ti_3AlC_2 MAX phase was slowly added to 20 mL of HF (49 wt%, Sigma Aldrich) in a Teflon beaker. The reaction mixture was stirred at 35 °C for 24 h using a magnetic stirrer with a Teflon bar. After the selective etching reaction, the sediment was washed by repeated centrifugation at 3500 rpm for 5 min using 40 mL of deionized H_2O. Then, the acidic supernatant was decanted, and the process was repeated until the pH reached neutral. The obtained sediment was separated from the deionized H_2O by vacuum filtering and dried at 80 °C for 2 h under vacuum.

2.2 Annealing of the MXene powder

For H_2 annealing, 1 g of the obtained multilayered MXene powder was inserted into the furnace, then heated to 750 °C under H_2 gas (99.9999%) with a pressure of 101 kPa and was maintained under these conditions for 2 h. The chamber and pot of the furnace used for H_2 annealing were made of Inconel steel to prevent brittle fracture of the metal by H_2 gas at high temperature. For the reduction of the MXene powder, Ca granules (purity: 99.5%, mean size: 2–5 mm) from Junsei (Japan) were used as the reduction agent. Multilayered MXene powder (1g) underwent heat treatment with Ca (molar ratio of 2:1) under a vacuum of 6.7×10^{-3} Pa at 750 °C for 2 h. After heat treatment, most of the Ca granules mixed with the MXene powder were clearly separated, and fine Ca and CaO were removed by washing with deionized H_2O. The obtained MXene powder was recovered by vacuum filtering and drying at 70 °C for 1 h under vacuum.

2.3 Fabrication of lithium-ion half-cell battery

Electrodes were fabricated by blending MXene powder with carbon black as a conductive agent and polyvinylidene difluoride as binder at a weight ratio of 8:1:1. This was mixed in a ratio of X:Y with N-Methyl-2-pyrrolidone (Sigma Aldrich) as the solvent. The electrolyte was 1.2 M of LiPF6 in a 1:1 (v/v, %) solution of ethylene carbonate and dimethyl carbonate. The electrode sheet was fabricated using a micrometer film applicator to apply the electrode slurry onto a Cu-foil substrate. The fabricated half-cell was prepared in the form of a CR2032 coin cell.

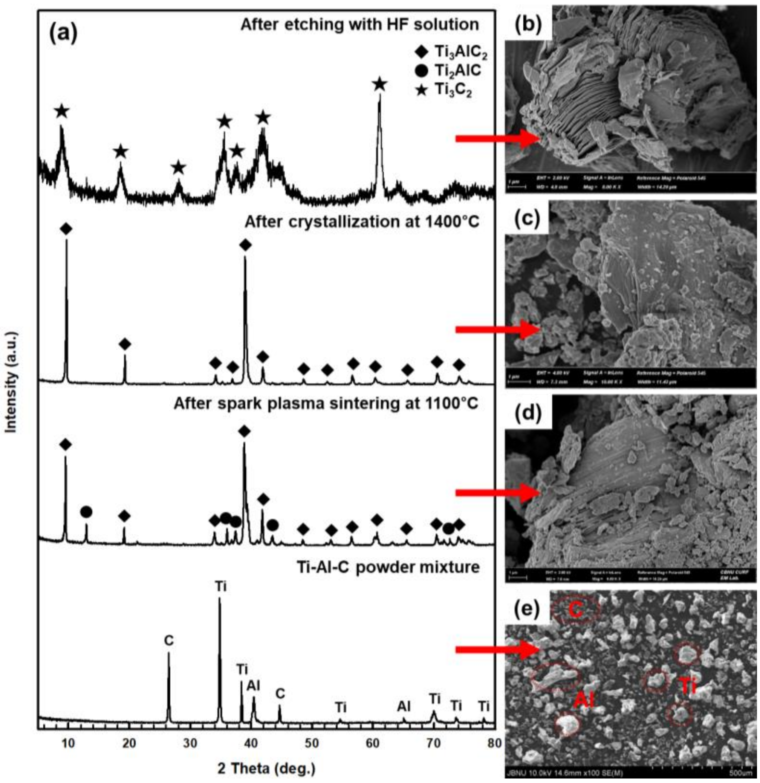

Fig. 1 (a) XRD patterns of MAX powder fabricated by SPS crystallization from Ti–Al–C powder mixture, and MXene powders obtained after HF etching to remove Al. FE-SEM images of (b-d) powder obtained by each process and (e) Ti–Al–C powder mixture.

2.4 Characterization

X-ray diffraction (XRD; XRD-6100, Shimadzu, Japan) and X-ray photoelectron spectroscopy (XPS; Escalab 250, Thermo Fisher Scientific, USA) were used to analyze the lattice parameters and chemical composition of the samples, respectively. In the case of O, the concentration was specifically measured using an O/N analyzer (ON-900, Eltra, Germany) and compared with the XPS results. The microstructural evolution was observed by field-emission scanning electron microscopy (FE-SEM; SUPRA40VP, Carl Zeiss, Germany) and transmission electron microscopy (TEM; JEM-2100, JEOL, Japan). UV-vis absorbance spectra of MXene dispersions with a mass concentration of 0.1 mg/mL were measured using an UV-vis-NIR spectrophotometer (Cary 5000 UV-Vis-NIR, Agilent, USA). A Brunauer–Emmett–Teller analyzer (BET; Trista-3000, Micromeritics Instrument, USA) was used to examine the SSA. Differential thermal and thermal gravimetric (DT/TG) analysis was performed at a heating rate of 3 °C/min up to 1000 °C in ambient atmosphere to observe changes in the high-temperature oxidation behavior using a thermal analyzer (DTG-60, Shimadzu, Japan). The electrochemical properties of the half-cell battery were evaluated using a WonATech battery tester (Korea). Galvanostatic charge–discharge tests of the half-cell battery were performed over the potential range of 0.1–3.0 V. The half-cell battery was evaluated at various C-rates (0.2, 0.5, 1, and 2 C). The cycle retention of the half-cell battery at 50 cycles was also evaluated. Electrochemical impedance spectroscopy (EIS) was performed with an amplitude of 10 mV from 10 mHz to 100 kHz.

3. Results and discussion

Fig. 1a shows the XRD patterns of the Ti–Al–C powder mixture, MAX powder obtained by SPS, MAX powder after crystallization, and MXene powder acquired after etching to eliminate Al. After SPS, the XRD pattern reveals that two phases, Ti_3AlC_2 and Ti_2AlC, were present. The subsequent powder was crystallized through an additional heat treatment at 1400 °C under vacuum to obtain a single Ti_3AlC_2 phase. The aim of this two-step sintering process is to first sinter at a low temperature and then crystallize the material at 1400 °C under vacuum to prevent Al from being removed when the temperature is raised to 1400 °C in a single process. This is a result of the significant difference in vapor pressure of Al and Ti (16.9 Pa and 4.82×10^{-3} Pa, respectively) at 1400 °C. The XRD patterns show that a single phase of Ti_3AlC_2 was successfully obtained after the crystallization at 1400 °C, and no significant Al peak was observed. Multilayered MXene powder was obtained by eliminating Al from the prepared MAX powder with the Ti_3AlC_2 phase using an HF solution via the selective etching of Al. The XRD pattern of the resulting MXene powder revealed that a single phase of Ti_3C_2 was produced by Al etching. Each obtained MXene layer is connected by a hydrogen bond or a weak van der Waals force (Gogotsi and Anasori 2019), which enables the delamination of the

Table 1 Gibbs free energy of each oxidation reaction according to temperature and the oxygen partial pressure at 750 °C

Oxide reaction	ΔG° at temperature (kJ/mol)				PO_2 at 750 °C (atm)
	550 °C	650 °C	750 °C	850 °C	
$2C + O_2 = 2CO$	- 360	- 380	- 400	- 420	1×10^{-19}
$C + O_2 = CO_2$	- 400	- 395	- 390	- 385	1×10^{-19}
$2H_2 + O_2 = 2H_2O$	- 405	- 390	- 375	- 365	1×10^{-19}
$Ti + O_2 = TiO_2$	- 780	- 760	- 745	- 725	1×10^{-37}
$4/3Al + O_2 = 2/3Al_2O_3$	- 930	- 910	- 885	- 865	1×10^{-45}
$2Ca + O_2 = 2CaO$	- 1110	- 1090	- 1075	- 1055	1×10^{-54}

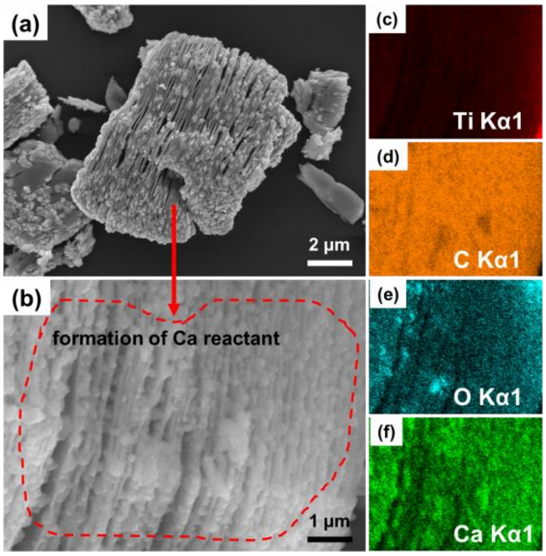

Fig. 2 (a) and (b) FE-SEM image and (c-f) EDS elemental mapping results of MXene powder obtained by Ca annealing at 850 °C. EDS mapping was performed on the area marked in (b) with a red dotted line.

layers as needed. FE-SEM images of the Ti–Al–C powder mixture and those obtained by each process are shown in Fig. 1b–e.

Prior to the main fabrication experiments, preliminary tests were conducted to optimize the annealing temperature of the MXene powder. Table 1 shows the oxidation reaction that can occur in this experiment and the Gibbs free energy according to each temperature, derived from the Ellingham diagram. Oxidation of Ca has the lowest Gibbs free energy, implying that it can be used as an efficient reducing agent for the reduction of MXene. The reduction effect using Ca is maximized when annealing is conducted above the melting temperature of Ca (830 °C) (Oh *et al*. 2012).

However, in the preliminary experiment, when the annealing was performed at 850 °C, small reactant particles were evenly spread on the surface of MXene (Fig. 2a and b). According to the EDS elemental maps obtained from the area marked with a red dotted line in Fig. 2b (Fig. 2c–f), Ca-containing reactants were formed. The reactants were probably calcium carbonate or oxide, both of which are unfavorable as they reduce the electrical conductivity of the MXene. Therefore, for further experiments, a lower temperature (750 °C) than the melting temperature of Ca was used. We confirmed that no reactants were generated under these conditions.

Henceforth, the MXene samples after etching in HF solution, after H_2 annealing, and after Ca annealing are denoted as HF-MXene, H_2-MXene, and Ca-MXene, respectively. Fig. 3a–d show FE-SEM images of the MAX, HF-MXene, H_2-MXene, and Ca-MXene powders, respectively. Fig. 3a shows that a layered MAX powder was obtained by the two-step SPS crystallization process. In Fig. 3b, each layer in the MXene was clearly separated, with an accordion-like structure after HF etching. There were no further significant changes in the morphology of the MXene after either annealing process (Fig. 3c and d). The XRD patterns of the MAX powder with the Ti_3AlC_2 phase and HF-MXene, H_2-MXene, and Ca-MXene with the Ti_3C_2 phase are shown in Fig. 3e and f. In the XRD pattern of the HF-MXene, a considerable loss in crystallinity and structural order compared to the MAX phase was observed. The (002) peak in the MAX phase broadened and shifted to a lower angle after HF etching, indicating an increase in the *d*-spacing in the HF-MXene. The shifts in the *d*-spacing, and lattice parameters, after each processing step are summarized in Fig. 3g. Changes in these parameters are caused by the removal of the Al layer from the Ti_3AlC_2 phase by HF etching. In addition, a small peak corresponding to TiO_2 was observed in the XRD patterns of the HF-MXene, which was produced by the local heat generated during HF etching (Rakhi *et al*. 2015). For H_2-MXene and Ca-MXene, the (002) peak shifted to a lower angle and the *d*-spacing further increased compared with those of HF-MXene. The *d* values of H_2-MXene and Ca-MXene were 0.993 nm and 0.998 nm, respectively. The *c* values of H_2-MXene and Ca-MXene were 1.984 nm and 1.996 nm, respectively. This clearly indicates that the interlayer spacing of MXene increased upon annealing under H_2 and Ca reduction. In particular, the interlayer spacing of the Ca-MXene was larger than that of other types of MXene, suggesting the removal of functional groups from the sample. The intensities of the TiO_2 peaks were the highest for H_2-MXene, which seemed to react with the trace amounts of O_2 gas in the atmosphere during H_2 annealing. Since H_2 annealing cannot be performed under high vacuum as a gas flow is required, it is difficult to prevent partial oxidation of metals with high oxygen affinity. Similar trends were also observed in the H_2 annealing of Ti-based alloy powder (Oh *et al*. 2014). Because TiO_2 was observed for all MXenes, it is thought to have mainly formed during HF etching, with some further oxidation occurring during H_2 annealing. In particular, from the large increase in the intensity of the TiO_2 peak at approximately 43°, it seems that the metastable anatase phase transformed to rutile during annealing, as the latter is more stable at high temperature. In contrast, in the MXene powder subjected to Ca reduction, the intensity of the TiO_2 peaks did not change significantly compared to the HF-MXene. Nevertheless, for all MXenes, TiO_2 peaks were observed, so further detailed analyses were performed using XPS and O/N analysis.

Fig. 4a shows XPS patterns of the MAX, HF-MXene, H_2-MXene, and Ca-MXene powders. The elemental concentrations derived from the XPS analyses for all

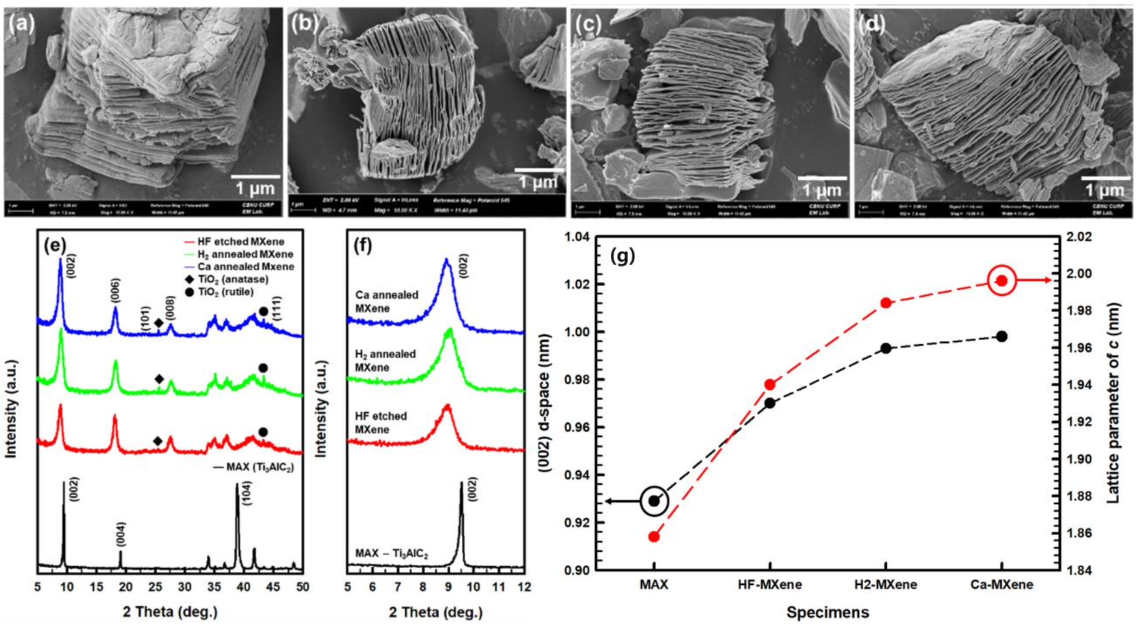

Fig. 3 FE-SEM images of (a) MAX (Ti_3AlC_2), (b) MXene ($Ti_3C_2T_x$) after etching in HF solution (HF-MXene), (c) MXene after annealing under H_2 atmosphere (H_2-MXene) and (d) MXene after annealing with Ca (Ca-MXene). XRD patterns of the MAX, HF-MXene, H_2-MXene, and Ca-MXene for (e) a wide angular range and (f) enlarged view around the main (002) peak. (g) Lattice parameters from XRD patterns of MAX, HF-MXene, H_2-MXene, and Ca-MXene.

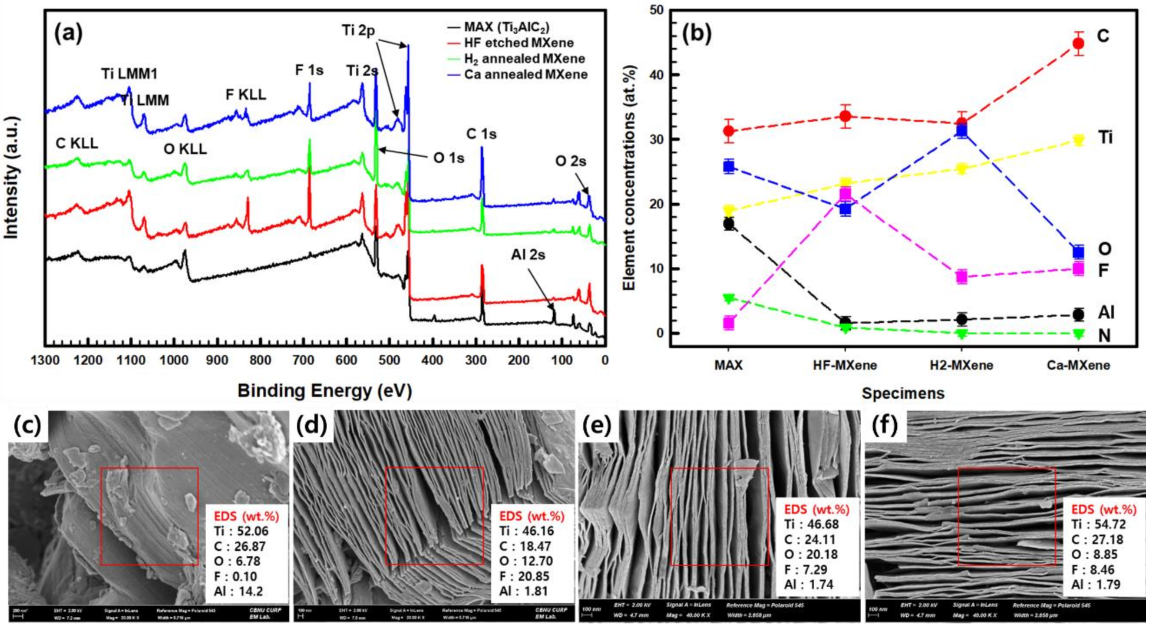

Fig. 4 (a) XPS profiles and (b) elemental concentrations of the MAX, HF-MXene, H_2-MXene, and Ca-MXene samples. FE-SEM images and EDS profiles for (c) MAX, (d) HF-MXene, (e)H_2-MXene, and (f) Ca-MXene.

samples are shown in Fig. 4b and Table 2. In HF-MXene, almost no Al was detected, while the F content significantly increased compared to that of MAX. Since the HF-based solution was used to remove Al from the MAX phase, an increase in F content in the MXene was inevitable. The F content of 21.54 at% in HF-MXene decreased to 8.71 at% after H_2 annealing. It has been reported that F on the surface of MXene is easily removed by H_2 annealing or vacuum heat treatment (Lu *et al.* 2019, Rakhi *et al*. 2015, Lee *et al*. 2020, Kong *et al*. 2018). However, after H_2 annealing, the O content greatly increased to 31.28 at% (from 19.25 at% for HF-MXene). This indicates that, contrary to expectation, H_2 annealing was not very effective for removing O from MXene. However, after Ca annealing, Ca-MXene showed a decrease in the O content from 19.25 at% to 12.51 at% as a result of the reduction effect of Ca due to its high O affinity. The F content was simultaneously reduced from 21.54 at% to 9.98 at%, which is attributed to the high-vacuum

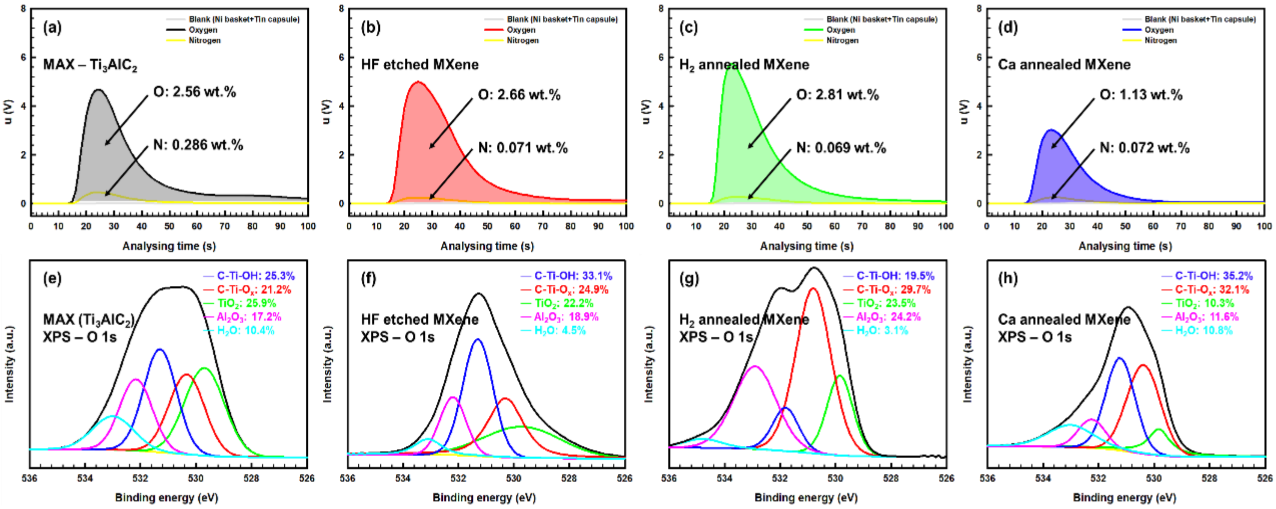

Fig. 5 Concentration of O and N in (a) MAX, (b) HF-MXene, (c) H_2-MXene, and (d) Ca-MXene measured by O/N analysis. Component peak-fitting of XPS O 1s spectra: (e) MAX, (f) HF-MXene, (g) H_2-MXene, and (h) Ca-MXene.

Table 2 XPS element concentrations of MAX, HF-MXene, H_2-MXene and Ca-MXene

	Element concentrations (at%)					
	Al	C	N	Ti	O	F
MAX	16.94	31.25	5.51	18.94	25.78	1.57
HF-MXene	1.57	33.55	0.9	23.18	19.25	21.54
H_2-MXene	2.11	32.45	-	25.44	31.28	8.71
Ca-MXene	2.85	44.79	-	29.86	12.51	9.98

conditions used for Ca annealing. The Ca-MXene sample showed the highest content of Ti and C, which is known to improve the electrical properties of MXene (Rakhi *et al.* 2015). The elemental concentrations from SEM–EDS analyses of all samples are shown in Fig. 4c-f. The results of the SEM-EDS analysis were in good agreement with those of the XPS results.

Further detailed quantitative analysis of the O concentration in the MAX and MXene powders was performed using an induced melting method with O/N analysis and XPS. Unlike XPS, which analyzes only the surface of the powder, the O/N analyzer completely melts the sample and reacts the released O with the internal C to measure its concentration with an infrared cell. Since the O/N analyzer only calculates the absolute amount of O and N through their reactants, the content of other elements cannot be measured. Instead, since the absolute amount of O and N in the entire sample can be measured, meaningful data can be derived when compared with the measurement of the relative content of elements obtained via XPS or EDS. In practice, this method is used to analyze the actual O concentrations in metals and ceramics. The concentrations of O and N measured by the O/N analyzer for all samples are shown in Fig. 5a–d.

The results showed that the O concentration of the MAX powder was 2.56 wt%, which increased to 2.66 wt% after HF etching, and further increased to 2.81 wt% after H_2 annealing. However, the O concentration of the Ca-MXene powder decreased to 1.13 wt% via the Ca reduction effect. These results were broadly consistent with the results of XPS, but there was a difference in the case of HF-MXene. The XPS results showed that the O concentration in the HF-MXene was slightly lower than that of the MAX powder, whereas it was slightly higher when determined by O/N analysis. This difference is caused by that the F content increasing significantly during HF treatment, resulting in a relative decrease in the O content determined by XPS. However, the O/N analysis confirmed that the O concentration actually increased after HF treatment. This indicates that attention should be paid to the technique when analyzing the O concentration of compounds such as MXene. Fig. 5 confirms that, unlike H_2 annealing, the O concentration in the MXene clearly decreased after Ca annealing. Additionally, similar to the XPS results, the N content was much lower than that of MAX for all MXene samples. This is favorable because N can cause internal strain in the lattice structure (Ramirez-Gonzalez *et al.* 2020). To investigate the differences in the O content between MAX, HF-MXene, H_2-MXene, and Ca-MXene, the XPS (O1s) spectra are shown in Fig. 5e–h. The O group in the MAX and multilayered MXene powder was mainly present as C–Ti–OH, C–Ti–O_x, TiO_2, Al_2O_3, and H_2O. The HF-MXene powder consisted of the same five components. The OH and O existed as termination groups in the C–Ti structure of MXene (Ti_3C_2), and a small amount of H_2O was attached to the surface. In addition, metal oxides in the form of TiO_2 and Al_2O_3 were present. Further, TiO_2 was detected in the XRD patterns of the MXene powders (Fig. 5e), but Al_2O_3 was not detected. This was presumably because the Al_2O_3 (113) peak around 43° overlaps the TiO_2 (111) peak. Al_2O_3 is known to form by reaction between O from the HF solution and Al that has not been completely removed during the MAX etching process (Scheibe *et al.* 2019). The volume fractions of TiO_2 and Al_2O_3 increased (Fig. 5g), while the total O concentration increased (Fig. 5c) after H_2 annealing because of the introduction of O_2 gas in the H_2 annealing atmosphere. Finally, in the case of Ca-MXene, the volume fraction of surface termination groups (–OH, –O) and adsorbed H_2O was a total of 78.1%. In particular,

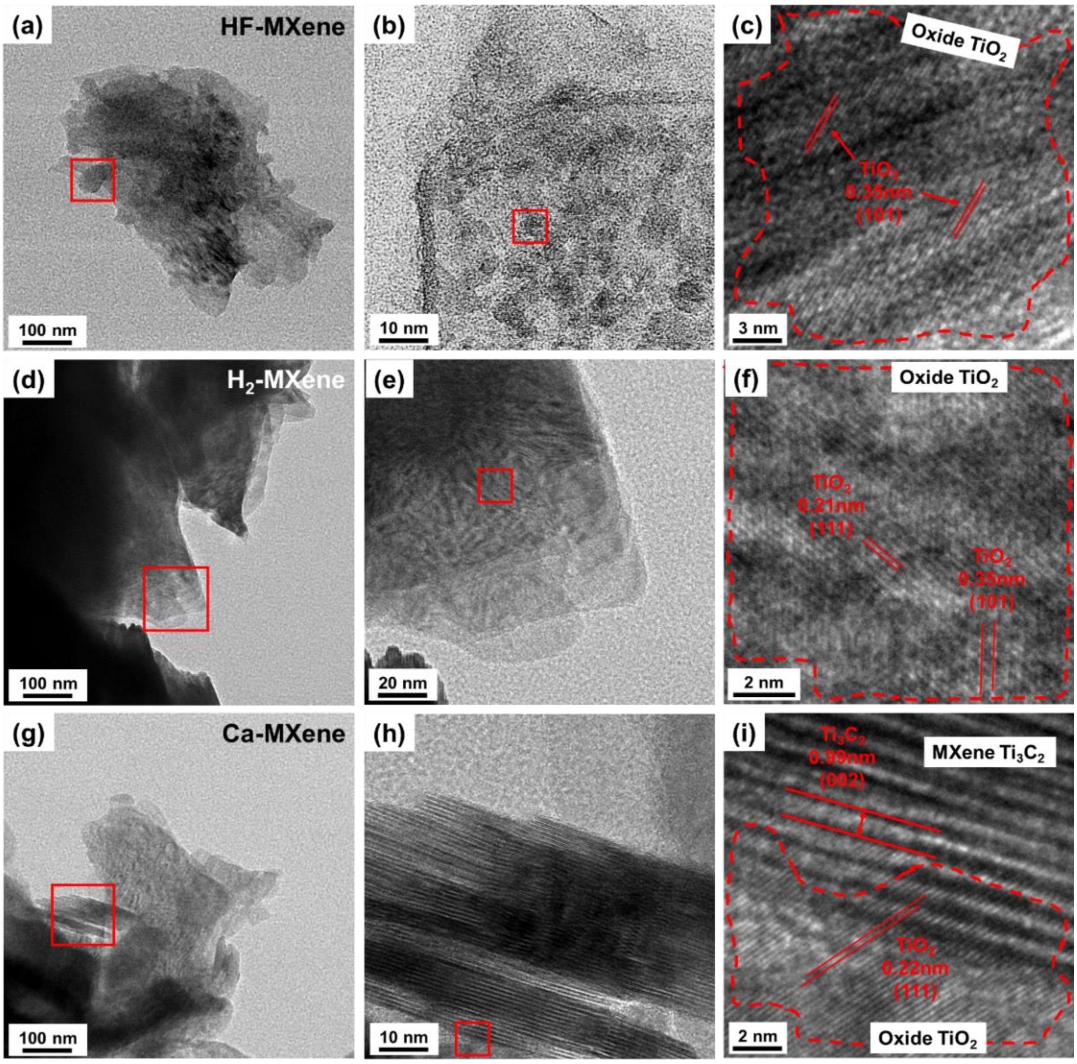

Fig. 6 TEM images of (a)-(c) HF-MXene, (d)-(f) H2-MXene, and (g)-(i) Ca-MXene.

the volume fractions of TiO_2 and Al_2O_3 notably decreased after Ca annealing, due to Ca having a higher affinity for oxygen than Ti or Al at the annealing temperature. The Gibbs free energy (ΔG^o) values for the oxidation of Ti, Al, and Ca are shown in Eq. (1)–(3), respectively, while those for the reduction reactions of TiO_2 and Al_2O_3 by Ca at 750 °C are shown in Eq. (4) and (5), respectively.

$$\Delta G^o\ (Ti + O_2 = TiO_2) = -745\ kJ/mol \tag{1}$$

$$\Delta G^o\ (4/3Al + O_2 = 2/3Al_2O_3) = -885\ kJ/mol \tag{2}$$

$$\Delta G^o\ (2Ca + O_2 = 2CaO) = -1075\ kJ/mol \tag{3}$$

$$\Delta G^o\ (TiO_2 + 2Ca = Ti + 2CaO) = -330\ kJ/mol \tag{4}$$

$$\Delta G^o\ (Al_2O_3 + 3Ca = 2Al + 3CaO) = -190\ kJ/mol \tag{5}$$

Both reduction reactions occur spontaneously because the ΔG^o values are negative. This indicates that our analyses are in good agreement with thermodynamic calculations.

TEM was used to examine the distribution of TiO_2 on the surface of the MXene samples. Fig. 6 shows TEM images of HF-MXene, H_2-MXene, and Ca-MXene particles. In these images, TiO_2 was located on the edge of MXene rather than on the wide plane. Unlike Ti metal particles, TiO_2 does not strongly bond to the surface and hence, it was sparsely distributed over the surface and edges of the MXene particles. It is expected that Al_2O_3 particles were also formed in a similar manner, and they were easily removed during sample preparation and did not appear on the TEM images. As shown in Fig. 6a–c, TiO_2 covered the MXene surface, and its inter-planar distance was 0.35 nm, which corresponds to the (101) plane of anatase. In contrast, the TiO_2 on the H_2-MXene surface has both anatase and rutile structure (Fig. 6d–f). As discussed above, it seems that two types of TiO_2 were present due to the phase transformation of some metastable anatase to the more-stable rutile structure at high temperatures. In the case of Ca-MXene (Fig. 6g–i), there were notable morphological changes in the TiO_2 phase on the surface and edges of the MXene particles after Ca annealing compared to HF-MXene and H_2-MXene. The overall area of TiO_2 decreased and it was mainly located on the edge of the MXene particles. The (111) plane of rutile was predominant.

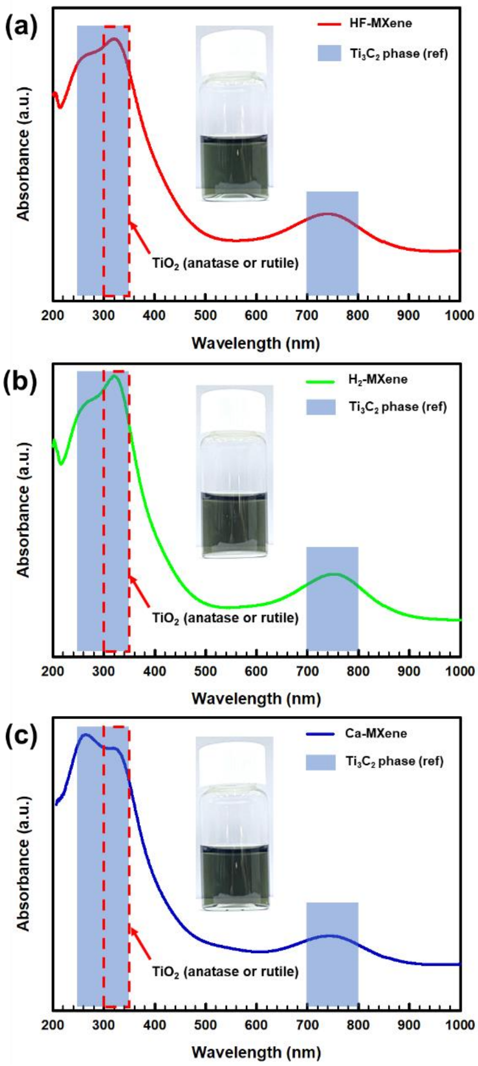

Fig. 7 UV-vis absorbance spectrum of (a) HF-MXene, (b) H_2-MXene, and (c) Ca-MXene dispersions with the same concentration (0.1 mg/mL).

UV-vis absorbance spectra of dispersions of HF-MXene, H_2-MXene, and Ca-MXene are shown in Fig. 7a–c, respectively. Each MXene powder was dispersed in deionized H_2O with a concentration of 0.1 mg/mL. In general, the main absorption bands of MXene (Ti_3C_2 phase) appear at wavelength ranges of 250–350 nm and 700–800 nm (Sarycheva *et al*. 2017). The bands identified for the dispersions of HF-MXene, H_2-MXene, and Ca-MXene matched these ranges well. However, as shown in Fig. 7(c), the peak at 300–350 nm for Ca-MXene had a lower intensity than those of the other samples. Given that the main spectrum of TiO_2 occurs in this wavelength range (Xiang *et al*. 2019), this is consistent with the lower content of TiO_2 in Ca-MXene. In addition, these spectra confirm that only single-phase Ti_3C_2 was dispersed in all samples; there was no discernable peak for Ti_2C (expected around 500–550 nm) (Shao *et al*. 2017).

The results of the previous analyses confirmed that –F generated from HF and oxygen groups containing –O and –OH first existed as surface termination groups on the initial MXene surface. Further, metal oxides such as TiO_2 and Al_2O_3 existed as oxygen-containing compounds. Although F can be easily removed by H_2 or Ca annealing at high temperatures, the concentration of O considerably increased during H_2 annealing, increasing the content of TiO_2 and Al_2O_3. These metal oxides increase the surface contact resistance of the MXene, resulting in a severe deterioration of its electrical properties. In contrast, during Ca annealing, the concentrations of both F and O decreased (corresponding to a decrease in TiO_2 and Al_2O_3 contents). In addition, the number of surface termination groups, such as –O and –OH, increased, which is expected to contribute to enhancing the hydrophilicity and adsorption properties of the MXene surface.

The changes in the fundamental properties of MXene by the modification of the surface groups were investigated by BET analysis. The N_2 adsorption and desorption isotherms of MAX, HF-MXene, H_2-MXene, and Ca-MXene powders are shown in Fig. 8a, giving BET SSA values of 1.63, 5.17, 9.45, and 10.98 m^2/g, respectively. The significant increase in the SSA after HF treatment indicates the successful removal of the Al layers from MAX due to the selective etching by HF. The isotherms of H_2-MXene and Ca-MXene had clear hysteresis loops in the range of 0.45–1.0 P/P_0, which indicate a mesoporous structure. This structure is consistent with that of typical multilayered MXene powder (Peng *et al*. 2018). MXene samples annealed in H_2 atmosphere and reduced with Ca had higher SSA values than that of HF-MXene, which may be due to the increase in the interlayer spacing after annealing and reduction (Rakhi *et al*. 2015). The pore volume distributions of the samples using the Barret–Joyner–Halenda (BJH) method are shown in Fig. 8b. The calculated pore volumes for the MAX, HF-MXene, H_2-MXene, and Ca-MXene powders were 0.0783, 0.2504, 0.4647, and 0.6093 cm^3/g, respectively. The large pore volume of Ca-MXene indicates its potential for achieving high volumetric energy density values when used for battery and capacitor applications.

To analyze the thermal stability of each MXene powder under ambient atmosphere, simultaneous DT/TG analysis was conducted from room temperature to 1000 °C (Fig. 8c and d). The MAX powder showed a typical TG curve for oxidation in air, where oxidation started at 250 °C and weight changes were observed up to 1000 °C. At 1000 °C, the weight of the MAX sample was 45% higher than the initial weight. In contrast, the MXene powders had completely different TG and DT behaviors. It has been reported that MXene goes through three stages in DT/TG analysis in air (Kong *et al*. 2018): (i) weight loss; (ii) rapid oxidation, and (iii) second weight loss. Step (i) is a result of the loss of physically adsorbed water or gases, while (ii) is due to the oxidation of C to CO_2, and (iii) is related to the removal of remaining surface functional F groups. For HF-MXene, an initial weight loss of 2.15% was observed between room temperature and ~280 °C due to the removal of surface moisture and gas. Due to the strong adsorption tendencies of MXene, this stage cannot be avoided. Subsequently, rapid oxidation commenced at about 300 °C, and the weight increased by 15.46%. According to the strong exothermic peak in the DT curve, MXene has

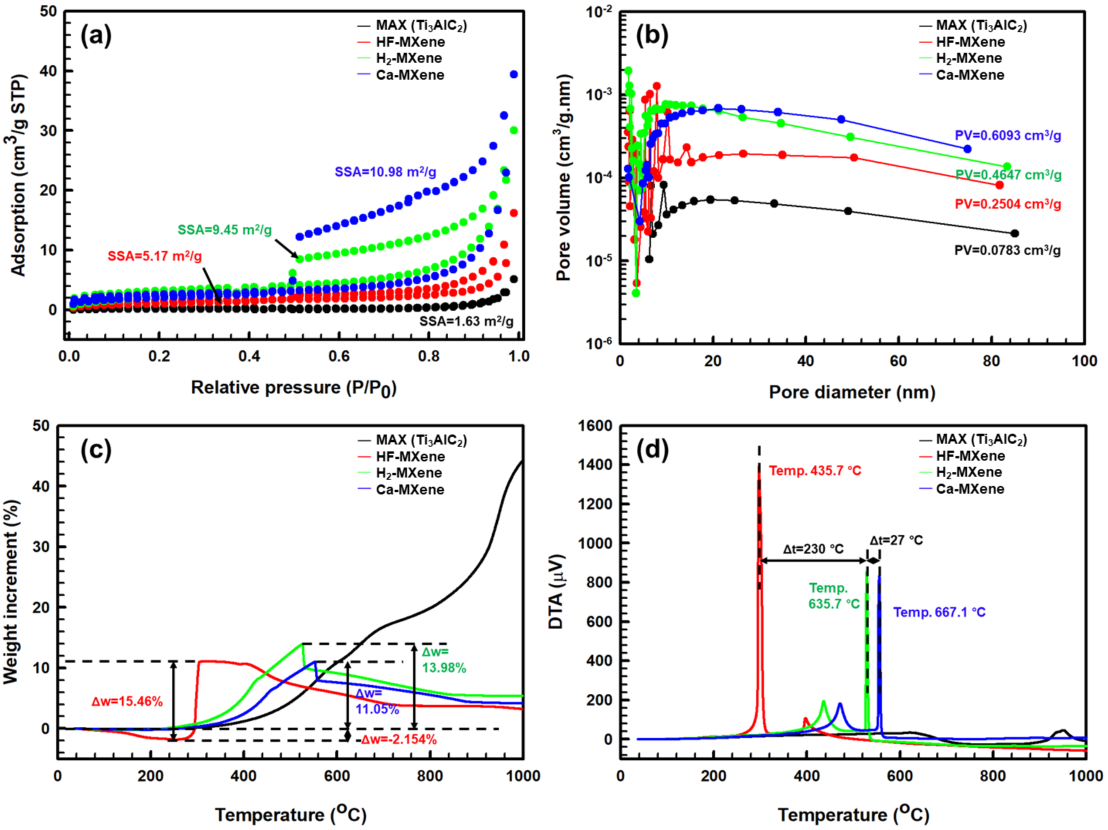

Fig. 8 (a) Nitrogen adsorption- desorption isotherms, (b) pore volume, (c) TG and (d) DTA curves for the MAX, HF-MXene, H_2-MXene, and Ca-MXene.

moderate thermal stability with an oxidation resistance temperature of 435.7 °C. Unlike HF-MXene, in the DT/TG analysis curves of H_2-MXene and Ca-MXene, no initial weight loss was observed. This is because the moisture or gases on the surface of the MXene were removed during the earlier heat treatments. The oxidation of the H_2-MXene started from approximately 200 °C and proceeded slowly, unlike the HF-MXene. According to the main exothermic peak in the DT curve, MXene had good thermal stability with an oxidation resistance temperature of 635.7 °C. Additionally, the oxidation of the Ca-MXene started from approximately 250 °C and proceeded very slowly. The weight gain of Ca-MXene occurred up to approximately 555 °C, increasing at a rate of 11.05%. As a result, the oxidation starting temperature of the Ca-MXene was raised to 250 °C, and the rate of weight gain was significantly lower than those of the other samples. This is attributed to the lower oxygen content of the MXene after Ca treatment. The supply of oxygen in the oxidizing environment was delayed because the total concentrations of O and metal oxide compounds attached to the surface were minimized during Ca annealing.

The use of MXene with a high SSA and thermal stability, as well as low F and oxide concentrations is expected to improve the performance of the lithium-ion batteries. To verify this, we applied the Ca-MXene to a lithium-ion battery and compared its performance to that of a battery using HF-MXene. The MXene electrodes were galvanostatically tested in half-cell configurations paired with Li metal as the counter electrode. Fig. 9a and b show the charge–discharge capacities of the half-cell battery at various C rates (0.1, 0.2, 0.5, and 1C) using the HF-MXene and Ca-MXene electrodes, respectively. The charge–discharge capacity profiles for both electrodes were similar from 0.1C to 1C. The two cells showed a similar discharge capacity of ~120 mAh/g at 1C (1st cycle). With increasing cycle numbers from the 1st to the 5th cycle at 1C, while the charge–discharge capacity profiles for Ca-MXene showed similar behavior, the capacity of HF-MXene decreased (at the same voltage). It is noted that the Ca-MXene electrode had higher electrochemical stability than that without Ca annealing (HF-MXene). The cycle tests of the battery using the MXene electrodes with and without Ca annealing were performed over 50 cycles at 1.0 C, as shown in Fig. 9c. In addition, the Coulombic efficiency of the battery after 50 cycles is also shown in Fig. 9c. The discharge capacity of the battery using Ca-MXene was 139.09, 121.99, and 111.19 mAh/g at the 1st, 25th, and 50th cycle, respectively, while that of the battery using HF-MXene was 132.03, 62.34, and 51.05 mAh/g, respectively. While the discharge capacity of the battery with the Ca-MXene slightly decreased up to the 8th cycle, and then showed linear behavior up to the 50th cycle, that of the battery with HF-MXene decreased significantly over 13 cycles, and then showed linear behavior up to the 50th cycle. Both batteries showed initial drops in the discharge during cycling (first ~10 cycles) due to irreversible reactions and formation of the solid electrolyte interphase (SEI) (Lv *et al*. 2014, Son *et*

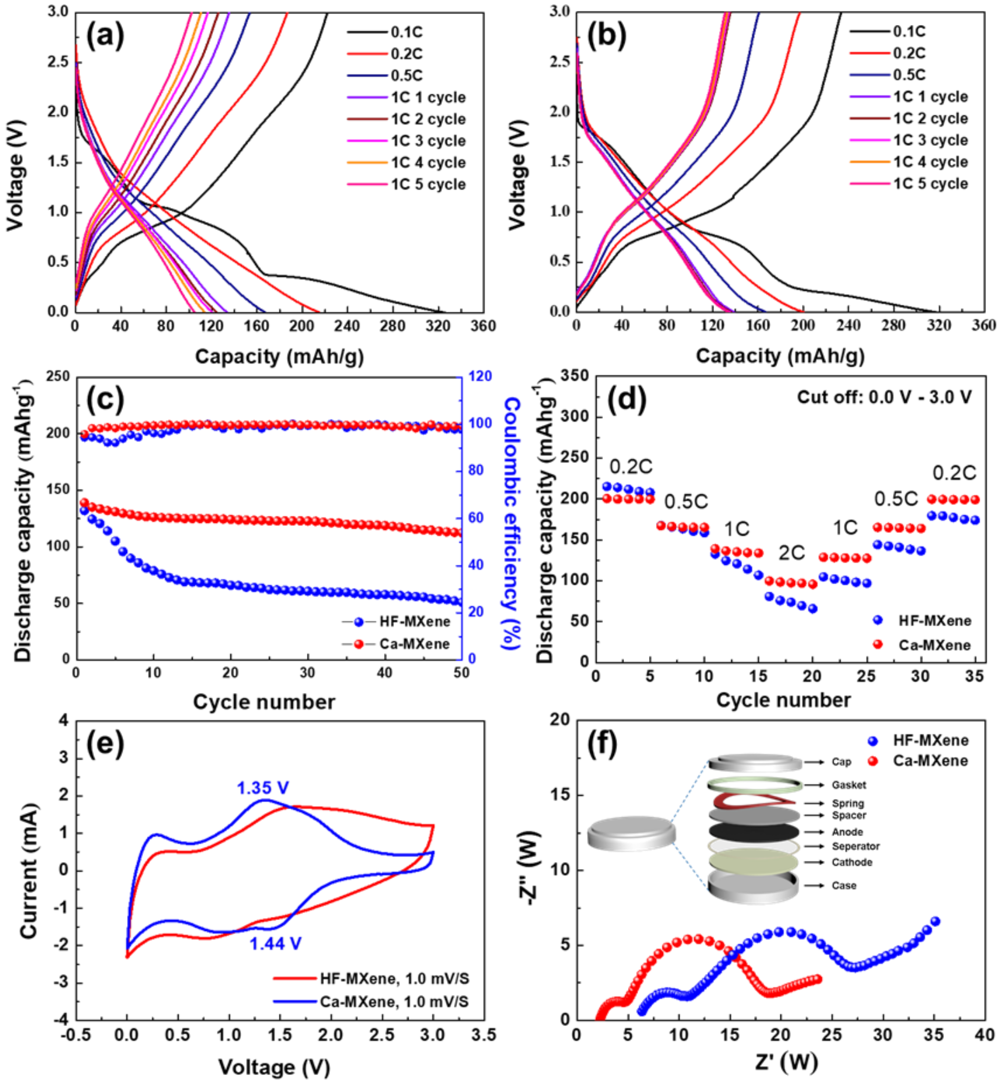

Fig. 9 Half-cell performance of batteries using HF-MXene or Ca-MXene electrodes. Charge–discharge capacities of the battery with (a) HF-MXene or (b) Ca-MXene at various C rates. (c) Discharge cycle retention at 1C and Coulombic efficiency of the battery using HF-MXene or Ca-MXene for 50 cycles. (d) Rate capability at various C rates of the batteries using HF-MXene or Ca-MXene. (e) Cyclic voltammetry profiles of the batteries using HF-MXene or Ca-MXene at 1 mVs-1. (f) Electrochemical impedance spectroscopy data of the batteries using HF-MXene or Ca-MXene. The inset figure is the structure of the fabricated lithium-ion half-cell battery.

al. 2014). From the cycle data, the performance of the battery with Ca-MXene was superior to that with HF-MXene. Similarly, the Coulombic efficiency of the Ca-MXene battery was superior to that of the HF-MXene one.

The rate capabilities of the batteries using HF-MXene or Ca-MXene electrodes were analyzed (Fig. 9d). The rate capability at various C rates (0.2C, 0.5C, 1C, 2C, 1C, 0.5C, and 0.2C) is shown for 5 cycles at each C rate. While the discharge capacities of the battery with the Ca-MXene electrode were steadily maintained at each C rate, those of the battery with HF-MXene decreased at each C rate. This reveals that the rate capability of the battery with Ca-MXene was superior to that with HF-MXene. Cyclic voltammetry (CV) curves of the half-cell batteries at 1 mVs^{-1} with or without Ca annealing were investigated over 50 cycles (Fig. 9e). In the case of the battery with Ca-MXene, strong anodic and cathodic peaks were observed at 1.35 V and 1.44 V, respectively, indicating the reversible alloying and dealloying processes, respectively. However, the CV data of the battery with HF-MXene showed no clear peaks, implying that the anodic and cathodic reactions were not strong and possible interfacial Li storage occurred via irreversible parasitic reactions (Choi *et al*. 2015). The results of EIS analysis of both batteries after 50 cycles are shown in Fig. 9f. Both electrodes showed two hemispherical arcs in the Nyquist plots. However, the charge-transfer resistance of the battery with Ca-MXene was much lower than that with HF-MXene after 50 cycles. The low interfacial resistance and enhanced charge-transfer kinetics of the Ca-MXene battery are attributed to the low F and oxide concentration and large SSA. This is the first report clarifying the effect of Ca annealing of electrodes on the charge–discharge performance of lithium-ion batteries. These findings are expected to contribute to the development of batteries using MXenes electrode in the near future.

4. Conclusions

We developed a novel Ca reduction method to improve the fundamental performance of the $Ti_3C_2T_x$ MXene by controlling its surface termination groups and metal-oxide content. In particular, because MXene surface termination groups with F and O strongly affect the conductivity, adsorption properties, SSA, and thermal conductivity of the electrode, the removal of F and O from the MXene surface was a priority. Unlike H_2 annealing, Ca annealing successfully removed O in addition to F, which favorably modified the MXene lattice structure and provided a larger SSA and pore density. Some of the decrease in O content in Ca-MXene was related to the reduction of TiO_2 and Al_2O_3, which improves the electrical properties of the MXene, and also delays the oxidation of MXene at high temperatures, consequently increasing its thermal resistance. Furthermore, surface termination groups such as –O and –OH are reinforced by Ca annealing, which is expected to enhance the hydrophilicity and adsorption properties of the MXene surface. As a result of this novel approach, the charge–discharge characteristics of a lithium-ion battery with Ca-MXene electrodes were considerably improved compared to a reference cell. To the best of our knowledge, the use of Ca reduction annealing to improve the properties of the MXene has not been reported previously. Considering the noticeable improvement in the performance of MXene after Ca annealing, this approach is expected to be highly beneficial for the development of highly efficient and stable batteries and supercapacitors that require good charge-transfer characteristics.

Acknowledgement

This work was supported by National Research Foundation of Korea (NRF) grants (Number 2020M3H 4A3081895, 2022R1A2C1010353 and RS-2023-00247545) funded by the Korean government (MSIP). Further support was provided by the Industry Technology R&D program (20006511), funded By the Ministry of Trade, Industry & Energy (MOTIE, Korea).

References

Ahn, S., Han, T.H., Maleski, K., Song, J., Kim, Y.H., Park, M.H., Zhou, H., Yoo, S., Gogotsi, Y., Lee, T.W. (2020), "A 2D titanium carbide MXene flexible electrode for high-efficiency light-emitting diodes", *Adv. Mater.*, **32**, 2000919. https://doi.org/10.1002/adma.202000919.

Chen, J., Li, Z., Ni, F., Ouyang, W., Fang, X. (2020), "Bio-inspired transparent MXene electrodes for flexible UV photodetectors", *Mater. Horizons*, **7**, 1828-1833. https://doi.org/10.1039/d0mh00394h.

Choi, S.H., Jung, K.Y., Kang, Y.C. (2015), "Amorphous GeOx-coated reduced graphene oxide balls with sandwich structure for long-life lithium-ion batteries", *ACS Appl. Mater. Interf.*, **7**, 13952-13959. https://doi.org/10.1021/acsami.5b02846.

Cai, M., Feng, P., Yan, H., Li, Y., Song, S., Li, W., Li, H., Zhu, M. (2022), "Hierarchical $Ti_3C_2T_x$@MoS_2 heterostructures: A first principles calculation and application in corrosion/wear protection", *J. Mater. Sci.*, **116**, 151-160. https://doi.org/10.1016/j.jmst.2021.11.026.

Cai, M., Fan, X., Yan, H., Li, Y., Song, S., Li, W., Li. H., Lu. Z., Zhu, M. (2021), "In situ assemble $Ti_3C_2T_x$ MXene@MgAl-LDH heterostructure towards anticorrosion and antiwear application", *Chem. Eng. J.*, **419**, 130050. https://doi.org/10.1016/j.cej.2021.130050.-2.

Cai, M., Yan, H., Song, S., He, D., Lin, Q., Li, W., Fan, X., Zhu, M. (2022), "State-of-the-art progresses for $Ti_3C_2T_x$ MXene reinforced polymer composites in corrosion and tribology aspects", *Adv. Colloid Interf. Sci.*, **309**, 102790. https://doi.org/10.1016/j.cis.2022.102790.-3.

Dall'Agnese, Y., Lukatskaya, M.R., Cook, K.M., Taberna, P.L., Gogotsi, Y., Simon, P. (2014), "high capacitance of surface-modified 2D titanium carbide in acidic electrolyte", *Electrochem. Commun.*, **48**, 118-122. https://doi.org/10.1016/j.elecom.2014.09.002.

Dong, Y., Zheng, S., Qin, J., Zhao, X., Shi, H., Wang, X., Chen, J., Wu, Z.S. (2018), "All-MXene-based integrated electrode constructed by Ti_3C_2 nanoribbon framework host and nanosheet interlayer for high-energy-Density Li-S batteries", *ACS Nano*, **12**, 2381-2388. https://doi.org/10.1021/acsnano.7b07672.

Fan, X., Yan, H., Cai, M., Song, S., Huang, Y., Zhu, M. (2022), "Achieving parallelly-arranged $Ti_3C_2T_x$ in epoxy coating for anti-corrosive/wear high-efficiency protection", *Compos. B. Eng.*, **231**, 109581. https://doi.org/10.1016/j.compositesb.2021.109581.

Fan, X., Yang, Y., Shi, X., Liu, Y., Li, H., Liang, J., Chen, Y. (2020), "A MXene-based hierarchical design enabling highly efficient and stable solar-water desalination with good salt resistance", *Adv. Funct. Mater.*, **30**, 2007110. https://doi.org/10.1002/adfm.202007110.

Fan, Z., Wang, Y., Xie, Z., Xu, X., Yuan, Y., Cheng, Z., Liu, Y. (2018), "A nanoporous MXene film enables flexible super-capacitors with high energy storage", *Nanoscale*, **10**, 9642-9652. https://doi.org/10.1039/c8nr01550c.

Feng, P., Ren, Y., Li, Y., He, J., Zhao, Z., Ma, X., Fan, X., Zhu, M. (2022), "Synergistic lubrication of few-layer $Ti_3C_2T_x/MoS_2$ heterojunction as a lubricant additive", *Friction*, **10**, 2018-2032. https://doi.org/10.1007/s40544-021-0568-3.

Gogotsi, Y., Anasori, B. (2019), "The Rise of MXenes", *ACS Nano*, **13**, 8491-8494. https://doi.org/10.1021/acsnano.9b06394.

Hu, M., Hu, T., Li, Z., Yang, Y., Cheng, R., Yang, J., Cui, C., Wang, X. (2018), "Surface functional groups and interlayer water determine the electrochemical capacitance of Ti_3C_2 T_x MXene", *ACS Nano*, **12**, 3578-3586. https://doi.org/10.1021/acsnano.8b00676.

Huang, Y., Yang, H., Zhang, Y., Zhang, Y., Wu, Y., Tian, M., Chen, P., Trout, R., Ma, Y., Wu, T.H., Wu, Y., Liu, N. (2019), "A Safe and Fast-Charging Lithium-Ion Battery Anode Using MXene Supported Li_3VO_4", *J. Mater. Chem. A*, **7**, 11250-11256. https://doi.org/10.1039/c9ta02037c.

Hwang, S.K., Kang, S. M., Rethinasabapathy, M., Roh, C., Huh, Y.S. (2020), "MXene: An emerging two-dimensional layered material for removal of radioactive pollutants", *Chem. Eng. J.*, **397**, 125428. https://doi.org/10.1016/j.cej.2020.125428.

Ihsanullah, I. (2020), "Potential of MXenes in water desalination: Current status and perspectives", *Nano-Micro Lett.*, **12**, 72. https://doi.org/10.1007/s40820-020-0411-9.

Iqbal, A., Sambyal, P., Koo, C.M. (2020), "2D MXenes for

Electromagnetic Shielding: A Review", *Adv. Funct. Mater.*, **30**, 2000883. https://doi.org/10.1002/adfm.202000883.

Jiang, Q., Kurra, N., Alhabeb, M., Gogotsi, Y., Alshareef, H. N. (2018), "All pseudocapacitive MXene-RuO_2 asymmetric supercapacitors", *Adv. Energy Mater.*, **8**, 1703043. https://doi.org/10.1002/aenm.201703043.

Kong, F., He, X., Liu, Q., Qi, X., Zheng, Y., Wang, R., Bai, Y. (2018), "Improving the electrochemical properties of MXene Ti_3C_2 multilayer for Li-Ion batteries by vacuum calcination", *Electrochim. Acta*, **265**, 140-150. https://doi.org/10.1016/j.electacta.2018.01.196.

Lee, Y., Kim, S.J., Kim, Y.J., Lim, Y., Chae, Y., Lee, B.J., Kim, Y.T., Han, H., Gogotsi, Y., Ahn, C.W. (2020), "Oxidation-Resistant Titanium Carbide MXene Films", *J. Mater. Chem. A*, **8**, 573-581. https://doi.org/10.1039/c9ta07036b.

Liu, J., Jiang, X., Zhang, R., Zhang, Y., Wu, L., Lu, W., Li, J., Li, Y., Zhang, H. (2019), "MXene-enabled electrochemical microfluidic biosensor: Applications toward multicomponent continuous monitoring in whole blood", *Adv. Funct. Mater.*, **29**, 1807326. https://doi.org/10.1002/adfm.201807326.

Lu, M., Li, H., Han, W., Chen, J., Shi, W., Wang, J., Meng, X. M., Qi, J., Li, H., Zhang, B., Zhang, W., Zheng, W. (2019), "2D Titanium Carbide (MXene) electrodes with lower-f surface for high performance lithium-ion batteries", *J. Energy Chem.*, **31**, 148-153. https://doi.org/10.1016/j.jechem.2018.05.017.

Lv, D., Gordin, M.L., Yi, R., Xu, T., Song, J., Jiang, Y. B., Choi, D., Wang, D. (2014), "GeO_x/reduced graphene oxide composite as an anode for li-ion batteries: Enhanced capacity via reversible utilization of Li_2O along with improved rate performance", *Adv. Funct. Mater.*, **24**, 1059-1066. https://doi.org/10.1002/adfm.201301882.

Malik, R. (2018), "Maxing out water desalination with MXenes", *Joule*, **2**, 591-593. https://doi.org/10.1016/j.joule.2018.04.001.

Munir, S., Rasheed, A., Rasheed, T., Ayman, I., Ajmal, S., Rehman, A., Shakir, I., Agboola, P.O., Warsi, M.F. (2020), "Exploring the influence of critical parameters for the effective synthesis of high-quality 2D MXene", *ACS Omega*, **5**, 26845-26854. https://doi.org/10.1021/acsomega.0c03970.

Naguib, M., Kurtoglu, M., Presser, V., Lu, J., Niu, J., Heon, M., Hultman, L., Gogotsi, Y., Barsoum, M. W. (2011), "Two-dimensional nanocrystals produced by exfoliation of Ti_3AlC_2", *Adv. Mater.*, **23**, 4248-4253. https://doi.org/10.1002/adma.201102306.

Natu, V., Clites, M., Pomerantseva, E., Barsoum, M.W. (2018), "Mesoporous MXene powders synthesized by acid induced crumpling and their use as Na-Ion battery anodes", *Mater. Res. Lett.*, **6**, 230-235. https://doi.org/10.1080/21663831.2018.1434249.

Nejadi, M.M., Mohammadimehr, M., Mehrabi, M. (2021), "Free vibration and buckling of functionally graded carbon nanotubes /graphene platelets Timoshenko sandwich beam resting on variable elastic foundation", *Adv. Nano Res.*, **10**(6), 539-548. http://doi.org/10.12989/anr.2021.10.6.539.

Oh, J.M., Kwon, H., Kim, W., Lim, J.W. (2014), "Oxygen behavior during non-contact deoxidation of titanium powder using calcium vapor", *Thin Solid Films*, **551**, 98-101. https://doi.org/10.1016/j.tsf.2013.11.076.

Oh, J.M., Lee, B.K., Suh, C.Y., Cho, S.W., Lim, J.W. (2012), "Preparation method of Ti powder with oxygen concentration of <1000 Ppm using Ca", *Powder Metall.*, **55**, 402-404. https://doi.org/10.1179/1743290112Y.0000000013.

Oh, J.M., Roh, K.M., Lee, B.K., Suh, C.Y., Kim, W., Kwon, H., Lim, J.W. (2014), "Preparation of low oxygen content alloy powder from Ti binary alloy scrap by hydrogenation-dehydrogenation and deoxidation process", *J. Alloys Compd.*, **593**, 61-66. https://doi.org/10.1016/j.jallcom.2014.01.033.

Peng, C., Wei, P., Chen, X., Zhang, Y., Zhu, F., Cao, Y., Wang, H., Yu, H., Peng, F. (2018), "a hydrothermal etching route to synthesis of 2D MXene (Ti_3C_2, Nb_2C): Enhanced exfoliation and improved adsorption performance", *Ceram. Int.*, **44**, 18886-18893. https://doi.org/10.1016/j.ceramint.2018.07.124.

Rakhi, R.B., Ahmed, B., Hedhili, M.N., Anjum, D.H., Alshareef, H.N. (2015), "Effect of postetch annealing gas composition on the structural and electrochemical properties of Ti_2CT_x MXene electrodes for supercapacitor applications", *Chem. Mater.*, **27**, 5314-5323. https://doi.org/10.1021/acs.chemmater.5b01623.

Ramirez-Gonzalez, D., Cruz-Rivera, J.J., Tiznado, H., Rodriguez, A.G., Guillen-Escamilla, I., Zamudio-Ojeda, A. (2020), "Caffeine as a source for nitrogen doped graphene, and its functionalization with silver nanowires in-situ", *Adv. Nano Res.*, **9**(1), 25-32. https://doi.org/10.12989/anr.2020.9.1.025.

Sarycheva, A., Makaryan, T., Maleski, K., Satheeshkumar, E., Melikyan, A., Minassian, H., Yoshimura, M., Gogotsi, Y. (2017), "Two-Dimensional titanium carbide (MXene) as surface-enhanced raman scattering substrate", *J. Phys. Chem. C*, **121**, 19983-19988. https://doi.org/10.1021/acs.jpcc.7b08180.

Scheibe, B., Kupka, V., Peplińska, B., Jarek, M., Tadyszak, K. (2019), "The influence of oxygen concentration during MAX phases (Ti_3AlC_2) preparation on the AAl_2O_3 microparticles content and specific surface area of multilayered MXenes (Ti_3C_2TX)", *Materials*, **12**, 353. https://doi.org/10.3390/ma12030353.

Schultz, T., Frey, N.C., Hantanasirisakul, K., Park, S., May, S.J., Shenoy, V.B., Gogotsi, Y., Koch, N. (2019), "Surface termination dependent work function and electronic properties of $Ti_3C_2T_x$ MXene", *Chem. Mater.*, **31**, 6590-6597. https://doi.org/10.1021/acs.chemmater.9b00414.

Shahzad, F., Alhabeb, M., Hatter, C.B., Anasori, B., Hong, S.M., Koo, C.M., Gogotsi, Y. (2016), "Electromagnetic interference shielding with 2D transition metal carbides (MXenes)", *Science*, **353**, 1137-1140. https://doi.org/10.1126/science.aag2421.

Shao, M., Yang, M., Shao, Y., Chai, J., Qu, Y., Yang, M., Wang, Z., Ip, W.F., Kwok, C.T., Shi, X., Lu, Z., Wang, S., Wang, X., Pan, H. (2017), "Synergistic Effect of 2D Ti_2C and G-C_3N_4 for efficient photocatalytic hydrogen production", *J. Mater. Chem. A*, **5**, 16748-16756. https://doi.org/10.1039/c7ta04122e.

Shen, C., Wang, L., Zhou, A., Zhang, H., Chen, Z., Hu, Q., Qin, G. (2017), "MoS_2-decorated Ti_3C_2 MXene nanosheet as anode material in lithium-ion batteries", *J. Electrochem. Soc.*, **164**, A2654-A2659. https://doi.org/10.1149/2.1421712jes.

Son, Y., Park, M., Son, Y., Lee, J.S., Jang, J.H., Kim, Y., Cho, J. (2014), "Quantum confinement and its related effects on the critical size of GeO_2 nanoparticles anodes for lithium batteries", *Nano Lett.*, **14**, 1005-1010. https://doi.org/10.1021/nl404466v.

Wang, Y., Li, Y., Qiu, Z., Wu, X., Zhou, P., Zhou, T., Zhao, J., Miao, Z., Zhou, J., Zhuo, S. (2018), "Fe_3O_4@Ti_3C_2 MXene hybrids with ultrahigh volumetric capacity as an anode material for lithium-ion batteries", *J. Mater. Chem. A*, **6**, 11189-11197. https://doi.org/10.1039/c8ta00122g.

Wen, Y., Rufford, T. E., Chen, X., Li, N., Lyu, M., Dai, L., Wang, L. (2017), "Nitrogen-doped $Ti_3C_2T_x$ MXene electrodes for high-performance supercapacitors", *Nano Energy*, **38**, 368-376. https://doi.org/10.1016/j.nanoen.2017.06.009.

Xiang, Q., Ma, X., Zhang, D., Zhou, H., Liao, Y., Zhang, H., Xu, S., Levchenko, I., Bazaka, K. (2019), "Interfacial modification of titanium dioxide to enhance photocatalytic efficiency towards H_2 production", *J. Colloid Interface Sci.*, **556**, 376-385. https://doi.org/10.1016/j.jcis.2019.08.033.

Yan, H., Fan, X., Cai, M., Song, S., Zhu, M. (2021), "Amino-functionalized $Ti_3C_2T_x$ loading ZIF-8 nanocontainer@ benzotriazole as multifunctional composite filler towards self-healing epoxy coating", *J. Colloid Interface Sci.*, **602**, 131-145. https://doi.org/10.1016/j.jcis.2021.06.004.

Yan, H., Zhang, L., Li, H., Fan, X., Zhu, M. (2020), "Towards high-performance additive of Ti_3C_2/graphene hybrid with a novel wrapping structure in epoxy coating", *Carbon*, **157**, 217-233. https://doi.org/10.1016/j.carbon.2019.10.034.

Yun, T., Kim, H., Iqbal, A., Cho, Y.S., Lee, G.S., Kim, M.K., Kim, S.J., Kim, D., Gogotsi, Y., Kim, S.O., Koo, C.M. (2020), "Electromagnetic shielding of monolayer MXene assemblies", *Adv. Mater.*, **32**, 1906769. https://doi.org/10.1002/adma.201906769.

Zhang, C.J., Anasori, B., Seral-Ascaso, A., Park, S.H., McEvoy, N., Shmeliov, A., Duesberg, G.S., Coleman, J.N., Gogotsi, Y., Nicolosi, V. (2017), "Transparent, flexible, and conductive 2D titanium carbide (MXene) films with high volumetric capacitance", *Adv. Mater.*, **29**, 1702678. https://doi.org/10.1002/adma.201702678.

Zhang, C.J., Nicolosi, V. (2019), "Graphene and MXene-Based transparent conductive electrodes and supercapacitors", *Energy Storage Mater.*, **16**, 102-125. https://doi.org/10.1016/j.ensm.2018.05.003.

Zhu, M., Huang, Y., Deng, Q., Zhou, J., Pei, Z., Xue, Q., Huang, Y., Wang, Z., Li, H., Huang, Q., Zhi, C. (2016), "Highly flexible, freestanding supercapacitor electrode with enhanced performance obtained by hybridizing polypyrrole chains with MXene", *Adv. Energy Mater.*, **6**, 1600969. https://doi.org/10.1002/aenm.201600969.

JL